Origins of bond and spin order in rare-earth nickelate bulk and heterostructures

Yi Lu,[1] Zhicheng Zhong,[1] Maurits W. Haverkort,[2,3] and Philipp Hansmann[1,4]
[1]*Max-Planck-Institut für Festkörperforschung, Heisenbergstrasse 1, 70569 Stuttgart, Germany*
[2]*Max-Planck-Institut für Chemische Physik fester Stoffe, Nöthnitzer Strasse 40, 01187 Dresden, Germany*
[3]*Institut für Theoretische Physik, Ruprecht-Karls-Universität Heidelberg, Philosophenweg 19, 69120 Heidelberg, Germany*
[4]*Institut für Theoretische Physik, Eberhard Karls Universität Tübingen, Auf der Morgenstelle 14, 72076 Tübingen, Germany*
(Received 12 October 2016; revised manuscript received 10 February 2017; published 9 May 2017)

We analyze the charge- and spin-response functions of rare-earth nickelates $R\mathrm{NiO_3}$ and their heterostructures using random-phase approximation in a two-band Hubbard model. The interorbital charge fluctuation is found to be the driving mechanism for the rock-salt-type bond order in bulk $R\mathrm{NiO_3}$, and good agreement of the ordering temperature with experimental values is achieved for all $R\mathrm{NiO_3}$ using realistic crystal structures and interaction parameters. We further show that magnetic ordering in bulk is not driven by the spin fluctuation and should be instead explained as ordering of localized moments. This picture changes for low-dimensional heterostructures, where the charge fluctuation is suppressed and overtaken by the enhanced spin instability, which results in a spin-density-wave ground state observed in recent experiments. Predictions for spectroscopy allow for further experimental testing of our claims.

DOI: 10.1103/PhysRevB.95.195117

I. INTRODUCTION

Understanding the mechanisms behind collective orders and excitations in solids is a pivotal topic in current condensed-matter research. The interplay between various electronic degrees of freedom at different time and energy scales gives rise to a virtually unlimited variety of properties such as metal-insulator transitions (MITs), multiferroicity, and superconductivity. One example of longstanding interest is the rare-earth nickelates $R\mathrm{NiO_3}$, which exhibit complex ordering phenomena depending on the $\mathrm{NiO_6}$ octahedra tilts and distortions controlled by the radius of rare-earth ion R [1–3]. For the smallest $R = \mathrm{Lu}$, $R\mathrm{NiO_3}$ goes through a MIT at $T_c \simeq 600$ K, accompanied by a rock-salt-type bond order of $\mathrm{NiO_6}$ octahedra at wave vector $\boldsymbol{q}_c = (1/2,1/2,1/2)$ (in units of $2\pi/a$ with a the pseudocubic lattice constant) with alternating Ni-O bond lengths. An antiferromagnetically ordered phase follows at much lower temperature $T_s \simeq 130$ K with an unusual $\boldsymbol{q}_s = (1/4,1/4,1/4)$. The temperature difference between the two transitions decreases with increasing R size and disappears at $R = \mathrm{Nd}$ with $T_c = T_s \simeq 200$ K. $\mathrm{LaNiO_3}$, with the largest R, remains metallic at all temperatures. This complex phase diagram can be further enriched by newly developed controlled growth of oxides with atomic precision [4]. Recent experiments have shown that via strain, dimensionality, and symmetry control in epitaxial films and heterostructures, the phase boundaries can be shifted and different order parameters can be selectively altered [5–13]. The quasi-two-dimensional heterostructures, for instance, show a pure spin-density-wave (SDW) ground state without bond order [8–10]—remarkably different from the bulk.

The complex phase behavior of the nickelates and the apparent dichotomy between the bulk and heterostructures pose several theoretical challenges archetypical for transition-metal oxides. The outstanding challenge is to understand the relation between the structural and electronic transitions. Recent discussions in the context of negative charge transfer insulators [14] have shown that the bond order is indispensable for understanding the MIT of the $R\mathrm{NiO_3}$. Constraining the system to the experimentally observed bond-ordered state, an insulating ground state was found in small-cluster [15,16], mean-field [15,17], and dynamical mean-field [18–20] calculations. However, the origin of the essential bond order, or its absence in low-dimensional heterostructures, has remained obscure.

In this paper, we address this crucial issue by examining—on equal footing—the charge- and spin-response functions in the unordered metallic phase for the $R\mathrm{NiO_3}$ series with multiorbital random phase approximation (RPA) [21,22] in a two-band Hubbard model. We identify a dominating charge response at $\boldsymbol{q}_c$ originated from interorbital fluctuations in the Ni-e_g states, which can drive the system into the bond order via strong electron-phonon coupling [23]. The instability increases with increasing $Pbnm$ (or $R\bar{3}c$ for $R = \mathrm{La}$) distortion and naturally explains the R dependence of the ordering temperature T_c in bulk $R\mathrm{NiO_3}$. The previously assumed primary spin instability [24,25], on the other hand, remains marginal in all bulk $R\mathrm{NiO_3}$. We further show that charge fluctuations are suppressed in spatially confined heterostructures below certain thickness, and a concomitant increase in the spin response can give rise to the experimentally observed SDW ground state without bond order [8–10].

II. HAMILTONIAN AND MULTIORBITAL RPA

We consider an effective two-band model [26] for the Ni-e_g orbitals

$$H = \sum_{\boldsymbol{k}\sigma ab} \epsilon_{\boldsymbol{k}ab} c^\dagger_{\boldsymbol{k}a\sigma} c_{\boldsymbol{k}b\sigma} + U \sum_{ia} n_{ia\uparrow} n_{ia\downarrow} + U' \sum_{i} n_{ia} n_{ib} + J \sum_{i\sigma\sigma'} c^\dagger_{ia\sigma} c^\dagger_{ib\sigma'} c_{ia\sigma'} c_{ib\sigma} + J' \sum_{i} c^\dagger_{ia\uparrow} c^\dagger_{ia\downarrow} c_{ib\downarrow} c_{ib\uparrow}, \tag{1}$$

where $c^\dagger_{ia\sigma}$ ($c^\dagger_{\boldsymbol{k}a\sigma}$) creates an electron at site i (momentum $\boldsymbol{k}$) in orbital a with spin $\sigma = \uparrow,\downarrow$. The orbital indices $a,b \in \{d_{3z^2-1}, d_{x^2-y^2}\}$ label the e_g Wannier functions. $\epsilon_{\boldsymbol{k}ab}$ is the

hopping matrix including the chemical potential. The number operators $n_{ia\sigma} = c^{\dagger}_{ia\sigma} c_{ia\sigma}$ and $n_{ia} = n_{ia\uparrow} + n_{ia\downarrow}$. The coupling constants U, U' denote the strength of intraorbital and interorbital Coulomb repulsion, and J, J' the intraorbital exchange and pair hopping. The RPA charge and spin susceptibilities are then given as

$$\hat{\chi}^{c/s} = \hat{\chi}^{0}(\mathbb{I} \pm \hat{\chi}^{0} U^{c/s})^{-1}, \quad (2)$$

where the matrix elements of the bare susceptibility $\hat{\chi}^{0}$ reads

$$\chi^{0}_{aa'bb'}(\boldsymbol{q}, i\Omega_n) = -\frac{1}{\beta} \sum_{\boldsymbol{k}m} G^{0}_{ab'}(\boldsymbol{k}, i\omega_m) G^{0}_{ba'}(\boldsymbol{k}+\boldsymbol{q}, i\omega'_m) \quad (3)$$

with $\beta = 1/T$ the inverse temperature and $G^{0}_{ab'}$ the bare Green's function. ω_m and $\omega'_m = \omega_m + \Omega_n$ are the fermionic Matsubara frequencies. U^{c} and U^{s} are the bare vertices coupling to charge- and spin-type of fluctuations, respectively, with matrix elements $U^{c}_{aa'bb'} = (U, -U' + 2J, 2U' - J, J', 0)$ and $U^{s}_{aa'bb'} = (U, U', J, J', 0)$ when $(a = a' = b = b'$, $a = b' \neq a' = b$, $a = a' \neq b = b'$, $a = b \neq a' = b'$ and otherwise). The total charge/spin susceptibility is then $\chi^{c/s} = \frac{1}{2}\sum_{ab}[\chi^{c/s}_{abba}]$.

While the interaction constants are often adopted as tuning parameters [21,22], it would be favorable to take parameters most relevant to the specific materials at hand. Such effective parameters can be calculated from first principles using the constrained RPA [27]. For $LuNiO_3$ the values in the e_g subspace are calculated by Seth *et al.* [28] as $U = 1.65$ eV, $J = 0.33$ eV, $U' = U - 2J$, and $J' = J$. These values are considerably smaller than the typical $RNiO_3$ bandwidth of $\sim$3 eV [29]—a parameter regime that RPA is well suited for. It is, however, important to note that RPA ignores crucial vertex corrections and overestimates the instabilities when using bare interaction parameters. Therefore we use the renormalized values given by the particle-particle vertex equation $\hat{\tilde{U}} = \hat{U}(\mathbb{I} + \hat{U}\hat{\Gamma}^{p})^{-1}$ with $\Gamma^{p}_{aa'bb'}(\boldsymbol{q}, i\Omega_n) = \frac{1}{\beta}\sum_{\boldsymbol{k}m} G^{0}_{ab'}(\boldsymbol{k}, i\omega_m) G^{0}_{ba'}(-\boldsymbol{k}+\boldsymbol{q}, i\omega'_m)$. Such an approach has been shown to reproduce correctly the exact susceptibilities obtained by quantum Monte Carlo methods in Hubbard models [30,31]. We arrive at static renormalized values at $T = 300$ K with $\bar{U} = 1.02$ eV, $\bar{U}' = 0.70$ eV, $\bar{J} = 0.17$ eV, and $\bar{J}' = 0.13$ eV by averaging over the $RNiO_3$ series. While the exact values of these parameters have a certain material and temperature dependence, we have checked that the variation does not change the results substantially. For simplicity we keep the interaction parameters fixed throughout this paper unless otherwise noted.

To study the structural dependence of charge- and spin-response functions, we performed calculations for the experimentally determined $RNiO_3$ structures in the $Pbnm$ or $R\bar{3}c$ metallic phase [32]. A hypothetical cubic $LaNiO_3$ [29] was also included as a reference system. The hopping matrices $\epsilon_{\boldsymbol{k}ab}$ are constructed using maximally localized Wannier orbitals [33] obtained from density functional (DFT) calculations [34]. To formulate the RPA calculation within a two-band model, the bare Green's functions are unfolded [35] to the pseudocubic Brillouin zone (BZ) for the noncubic cases.

We start by discussing the static noninteracting $\chi^{0}(\boldsymbol{q})$ for $LaNiO_3$ constrained to cubic symmetry shown in Fig. 1(a).

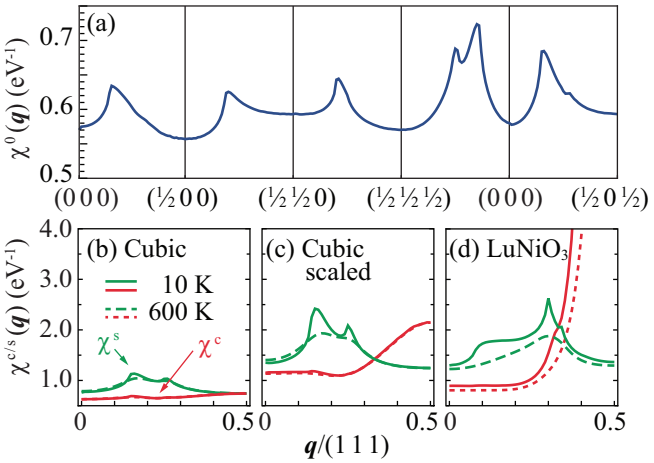

FIG. 1. (a) Static $\chi^{0}(\boldsymbol{q})$ along the high symmetry lines for cubic $LaNiO_3$ at $T = 10$ K. (b)–(d) Temperature dependence of $\chi^{c}(\boldsymbol{q})$ (red) and $\chi^{s}(\boldsymbol{q})$ (green) for (b) cubic $LaNiO_3$ with original and (c) scaled bandwidth (see text), and (d) $LuNiO_3$.

In agreement with previous results [24,25], two maxima are found at incommensurate wave vectors around $\boldsymbol{q}_s$. Their transition to the commensurate $\boldsymbol{q}_s$ can occur due to the spin-lattice coupling or simply by adopting hopping parameters better describing the experimentally measured Fermi surface [24], and therefore we refer to them as $\boldsymbol{q}_s$ hereafter. In a single-band RPA description, the spin instability is expected to be dominating with repulsive U as χ^{0} is positive and χ^{s} scales with $(1 - \chi^{0}U)^{-1}$, while the charge response $\chi^{c} \propto (1 + \chi^{0}U)^{-1}$ is always suppressed. In the multiorbital case, however, this simple argument does not hold due to the matrix nature of Eq. (2). An increase of the charge response at $\boldsymbol{q}_c$—which corresponds to a minimum of $\chi^{0}(\boldsymbol{q})$—appears once the inter-orbital interaction U' is included [29]. Based on the observations that both $\chi^{c}(\boldsymbol{q})$ and $\chi^{s}(\boldsymbol{q})$ show instabilities at the respective experimental wave vectors for bond and magnetic order, one naturally poses the question of whether the dependence of χ^{s} and χ^{c} upon the $Pbnm$ (or $R\bar{3}c$ for unconstrained $LaNiO_3$) distortion can explain the material trend of phase transitions in the $RNiO_3$ series.

The distortions affect the material-dependent $\epsilon_{\boldsymbol{k}ab}$ in two distinctive aspects: (i) an overall reduction of bandwidth, and (ii) broken selection rules for orbital transitions due to lower symmetry. The effect of (i) on the response functions is shown in Figs. 1(b) and 1(c). Both $\chi^{s}(\boldsymbol{q})$ and $\chi^{c}(\boldsymbol{q})$ show a noticeable increase when the bandwidth of the cubic $LaNiO_3$ ($\approx$3.9eV) is reduced to that of orthorhombic $LuNiO_3$ ($\approx$2.7eV) [29]. Subsequently, we see the effect of (ii) when comparing the scaled cubic case to the actual calculation of $LuNiO_3$ shown in Fig. 1(d). While $\chi^{s}(\boldsymbol{q})$ changes slightly its momentum dependence without noteworthy increase of the overall response, $\chi^{c}(\boldsymbol{q})$ becomes dominant and approaches divergence at $\boldsymbol{q}_c$ below 600 K, which signals a phase transition to an ordered state with ordering vector $\boldsymbol{q}_c$, in agreement with experiment.

III. BULK PHASE DIAGRAM

Figure 2 shows an overview of the calculated temperature dependence of $\chi^{c}(\boldsymbol{q}_c)$ and $\chi^{s}(\boldsymbol{q}_s)$ for $RNiO_3$ with various

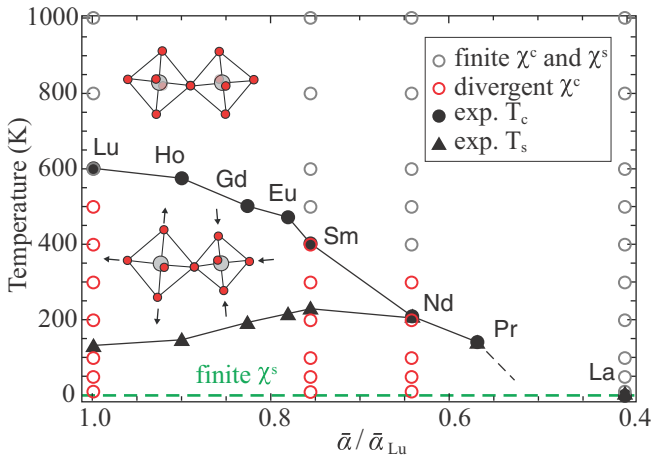

FIG. 2. Phase diagram of RNiO$_3$ with different distortions. $\bar{\alpha}$ is the averaged deviation of the Ni-O-Ni bond angle from 180°. The open circles mark the calculated data points, where red color indicates the divergence of $\chi^c(\boldsymbol{q}_c)$. $\chi^s(\boldsymbol{q}_s)$ remains finite at all temperatures, which is represented by a dashed line at $T = 0$. The experimental T_c (T_s) values [3] are denoted by black dots (triangles).

distortions in addition to the extremal case of LuNiO$_3$. The charge-response function $\chi^c(\boldsymbol{q}_c)$ dominates over the whole RNiO$_3$ series and the boundary of its divergence follows closely the experimental T_c, including the absence of a divergence/transition for LaNiO$_3$ down to the lowest considered temperature. (We note that a similar trend for the transition temperature was observed in more involved DFT plus dynamical mean-field calculations in Ref. [19].) The spin-response function $\chi^s(\boldsymbol{q}_s)$, on the other hand, remains finite for all materials throughout the full considered temperature range down to 10 K, which indicates a secondary role of spin fluctuations. We emphasize that this is also true for NdNiO$_3$—with experimentally equal T_c and T_s—which first and foremost undergoes a charge-driven transition. A direct consequence is that the subsequent magnetic transition should be understood starting from the insulating bond-ordered state (a more apparent statement for compounds with smaller R). Hence, instead of an itinerant approach based on Fermi liquid [24,25], the magnetic order in RNiO$_3$ may be more appropriately studied using a localized spin model. Another fact supporting this claim is the distortion dependence of the experimental T_s that increases with decreasing structural distortion (or increasing bandwidth), while an opposite trend should be expected if it is driven by $\chi^s(\boldsymbol{q}_s)$. In fact, in the part of the phase diagram where transition to the bond-ordered state and magnetic transition are separated, T_s is proportional to the exchange interaction $J_{ex} \sim W^2/\Delta$ given by perturbation theory, with W the bandwidth and Δ the characteristic charge excitation gap in the insulating phase defined by the Coulomb interaction and charge transfer energy. This is also confirmed by the energy gain of the antiferromagnetic state, which we calculated with constrained DFT+U [29] in the low-temperature monoclinic phase. The peculiar out-of-trend behavior of T_s for R = Nd and Pr is naturally explained since the magnetic order can only occur in the insulating bond-ordered state. This also explains the elevated T_s in a NdNiO$_3$ film when T_c is increased by epitaxial strain [11].

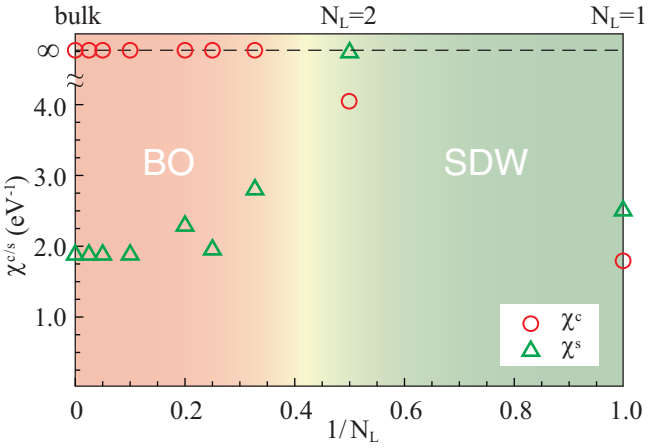

FIG. 3. Thickness N_L dependence of $\chi^c(\boldsymbol{q}_c)$ and $\chi^s(\boldsymbol{q}_s)$ at $T = 10$ K for NdNiO$_3$ with N_L = 1–5, 10, 20, and 40. The bulk ($1/N_L = 0$) values are plotted for comparison.

IV. EFFECT OF SPATIAL CONFINEMENT

After providing a unified description for the transitions in bulk RNiO$_3$ by identifying a dominating-bond-order picture, we are left with a puzzle as to how this is applicable to low-dimensional heterostructures, where magnetic order is observed without bond order [8–10]. To understand the dimensional effect we performed calculations for NdNiO$_3$ slabs with different thicknesses of N_L layers [29]. The lattice symmetry and hopping parameters were kept the same as the bulk, leaving the dimensionality as the only control parameter. The thickness dependence of $\chi^c(\boldsymbol{q}_c)$ and $\chi^s(\boldsymbol{q}_s)$ is shown in Fig. 3. For $N_L \geqslant 10$, the details of $\chi^{c/s}(\boldsymbol{q})$ remain largely unaffected compared to the bulk [29] with their respective maxima at $\boldsymbol{q}_c$ and $\boldsymbol{q}_s$ closely reproducing the bulk values. For N_L below 5, deviations from the bulk are noticeable in the details [29], and a dimensional crossover can be observed between $N_L = 3$ and 2, where $\chi^c(\boldsymbol{q}_c)$ is suppressed while $\chi^s(\boldsymbol{q}_s)$ becomes dominant and even diverges with $N_L = 2$. For $N_L = 1$, the system becomes two-dimensional with $\chi^c(\boldsymbol{q}_c^{\parallel})$ ($\parallel$ denotes the $\boldsymbol{q}$ projection in the layer plane) fully suppressed [29]. Interestingly, while $\chi^s(\boldsymbol{q}_s^{\parallel})$ remains dominating in single layer as in the bilayer, it does not diverge. (Note that in principle larger interaction parameters should be used for the two-dimensional case due to the less effective screening, which may still push $\chi^s(\boldsymbol{q}_s)$ and/or $\chi^c(\boldsymbol{q}_c)$ to divergence.) The difference might be attributed to a better nesting condition in the bilayer [29]. The seemingly contradicting observations in heterostructures are thus explained by the suppression of $\chi^c(\boldsymbol{q}_c)$ and enhancement of $\chi^s(\boldsymbol{q}_s)$ in reduced dimensions, although we note that the exact critical thickness N_L may differ for, e.g., different materials and/or epitaxial strains. These findings further prove the validity of our analysis and in addition point out an itinerant origin of the magnetism in heterostructures, qualitatively different from the bulk materials.

V. DYNAMICS OF THE CHARGE RESPONSE

The divergence of static susceptibilities yields information about critical parameters and symmetry of the phase transition to an ordered state. The frequency dependence of $\chi^{c/s}(\omega,\boldsymbol{q})$,

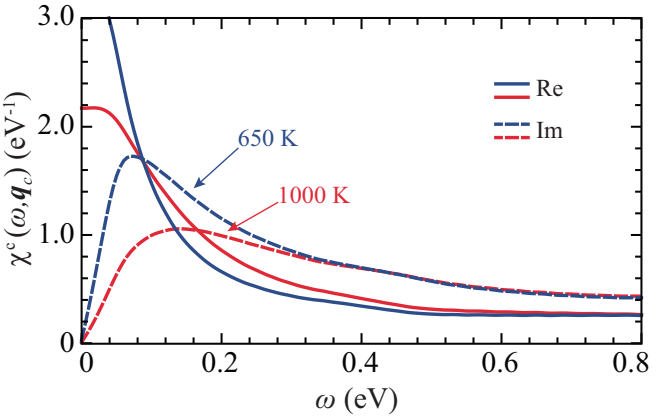

FIG. 4. Real (solid) and imaginary (dashed) parts of $\chi^c(\omega,\boldsymbol{q}_c)$ for $LuNiO_3$ at 1000 K (red) and 650 K (blue).

on the other hand, provides additional information about the evolution of the characteristic correlation time of a charge or spin fluctuation when approaching the phase transition. Such quantities, when experimentally accessible, can further strengthen or falsify our proposals. Figure 4 shows the real and imaginary part of $\chi^c(\omega,\mathbf{q}_c)$ for $LuNiO_3$ at two different temperatures above T_c. With decreasing temperature, the spectral weight of the imaginary part shifts to lower frequencies with a concomitant increase of the Kramers-Kronig-related real part at $\omega = 0$. At 650 K, a temperature close to $T_c \simeq 600$ K, the maximum of the peak is at 0.075 eV corresponding to a time scale of $\sim 10^{-13}$ s. This time scale is slower than that of core-level or optical spectroscopy on the order of a few to a dozen femtoseconds and should be detectable using such methods. Indeed, signs of dynamic valence fluctuation of Ni associated to the bond order was observed in $LuNiO_3$ above T_c using x-ray absorption [36]. The charge fluctuation was also indicated by the Fermi surface reconstruction with $\boldsymbol{q}_c$ observed in metallic $LaNiO_3$ films using angle-resolved photoemission [37]. Future resonant inelastic x-ray scattering (RIXS) experiments, which can measure the response functions directly in the frequency domain, may help to gain more quantitative information about the dynamics of the fluctuations and its relation to the phase transition.

VI. CLOSING REMARKS

In the following we discuss briefly the order of the transitions. Experimentally, the MIT in bulk $R NiO_3$ is weakly first order, and the magnetic transition is second order when separated from the first transition. Although the divergence of $\chi^c(\boldsymbol{q})$ is always an indication of a second-order transition, the observed first-order transition at T_c can be accounted for by considering its coupling to the lattice degrees of freedom [23] and the resulting bond order, as expected in, e.g., standard Landau theory [24,38]. RIXS measurement as mentioned above should give insights to the order of the transition. A divergence of spectral weight and collapse in energy at $\boldsymbol{q}_c$ should occur for a second-order transition when approaching the transition temperature from the metallic phase. For the heterostructures, the SDW transition was revealed to be second order [10], in agreement with our study.

A second remark is on the relation of our work to earlier approaches starting from the local limit, which include the O-p orbitals explicitly [15–18]. In the negative charge transfer picture, the oxygens donate one electron onto each Ni site in the metallic state. Upon bond order, the oxygen holes condensate onto half of the NiO_6 octahedra, which in the extreme case gives rise to a local $S = 0$ singlet state while the other half of the Ni sublattice develops into a Mott phase with $S = 1$. The traditionally termed "charge order" in the bond-ordered phase therefore does not involve actual charge redistribution on the Ni sites. Our current findings do not contradict this local many-body picture. The Ni e_g Wannier functions are composite objects including hybridized Ni-d states and the neighboring O-p states. While the divergence of $\chi^c(\boldsymbol{q}_c)$ in our calculation indicates a nearest-neighbor rock-salt-type charge order, the extended tails of the Wannier functions on the O sites ensure that a large part of the charge density does not move in space.

VII. CONCLUSION

We have presented a study of charge- and spin-response functions for the family of rare-earth nickelates $R NiO_3$. Within multiorbital RPA approach on an effective Ni-e_g model, we showed that the interorbital fluctuation increases with $Pbnm$ distortion and strongly contributes to the charge-response function $\chi^c(\boldsymbol{q})$ that is responsible for the observed bond order in bulk $R NiO_3$. The charge instability is suppressed in low-dimensional heterostructures, leaving magnetism to prevail, in agreement with recent experimental observations. The frequency dependence of the calculated charge response explains the dynamic charge fluctuation above the phase transition observed in x-ray absorption and photoemission experiments, and stands as a prediction for future experiments.

ACKNOWLEDGMENTS

We thank B. Keimer, E. Benckiser, X. Cao, M. Höppner, G. Khaliullin, and O. K. Andersen for motivation and fruitful discussions. We are especially grateful to authors of Ref. [28] for communicating us with cRPA results before publication.

[1] J. B. Torrance, P. Lacorre, A. I. Nazzal, E. J. Ansaldo, and C. Niedermayer, Phys. Rev. B **45**, 8209 (1992).
[2] M. L. Medarde, J. Phys. Condens. Matter **9**, 1679 (1997).
[3] G. Catalan, Phase Transitions **81**, 729 (2008).
[4] H. Y. Hwang, Y. Iwasa, M. Kawasaki, B. Keimer, N. Nagaosa, and Y. Tokura, Nat. Mater. **11**, 103 (2012).
[5] R. Scherwitzl, S. Gariglio, M. Gabay, P. Zubko, M. Gibert, and J.-M. Triscone, Phys. Rev. Lett. **106**, 246403 (2011).
[6] J. Liu, S. Okamoto, M. van Veenendaal, M. Kareev, B. Gray, P. Ryan, J. W. Freeland, and J. Chakhalian, Phys. Rev. B **83**, 161102 (2011).

[7] A. V. Boris, Y. Matiks, E. Benckiser, A. Frano, P. Popovich, V. Hinkov, P. Wochner, M. Castro-Colin, E. Detemple, V. K. Malik, C. Bernhard, T. Prokscha, A. Suter, Z. Salman, E. Morenzoni, G. Cristiani, H.-U. Habermeier, and B. Keimer, Science **332**, 937 (2011).

[8] A. Frano, E. Schierle, M. W. Haverkort, Y. Lu, M. Wu, S. Blanco-Canosa, U. Nwankwo, A. V. Boris, P. Wochner, G. Cristiani, H. U. Habermeier, G. Logvenov, V. Hinkov, E. Benckiser, E. Weschke, and B. Keimer, Phys. Rev. Lett. **111**, 106804 (2013).

[9] Y. Lu, A. Frano, M. Bluschke, M. Hepting, S. Macke, J. Strempfer, P. Wochner, G. Cristiani, G. Logvenov, H.-U. Habermeier, M. W. Haverkort, B. Keimer, and E. Benckiser, Phys. Rev. B **93**, 165121 (2016).

[10] M. Hepting, M. Minola, A. Frano, G. Cristiani, G. Logvenov, E. Schierle, M. Wu, M. Bluschke, E. Weschke, H.-U. Habermeier, E. Benckiser, M. Le Tacon, and B. Keimer, Phys. Rev. Lett. **113**, 227206 (2014).

[11] S. Catalano, M. Gibert, V. Bisogni, F. He, R. Sutarto, M. Viret, P. Zubko, R. Scherwitzl, G. A. Sawatzky, T. Schmitt, and J.-M. Triscone, APL Mater. **3**, 062506 (2015).

[12] J. Hoffman, I. C. Tung, B. B. Nelson-Cheeseman, M. Liu, J. W. Freeland, and A. Bhattacharya, Phys. Rev. B **88**, 144411 (2013).

[13] T. H. Kim, D. Puggioni, Y. Yuan, L. Xie, H. Zhou, N. Campbell, P. J. Ryan, Y. Choi, J. W. Kim, J. R. Patzner, S. Ryu, J. P. Podkaminer, J. Irwin, Y. Ma, C. J. Fennie, M. S. Rzchowski, X. Q. Pan, V. Gopalan, J. M. Rondinelli, and C. B. Eom, Nature (London) **533**, 68 (2016).

[14] T. Mizokawa, H. Namatame, A. Fujimori, K. Akeyama, H. Kondoh, H. Kuroda, and N. Kosugi, Phys. Rev. Lett. **67**, 1638 (1991).

[15] S. Johnston, A. Mukherjee, I. Elfimov, M. Berciu, and G. A. Sawatzky, Phys. Rev. Lett. **112**, 106404 (2014).

[16] R. J. Green, M. W. Haverkort, and G. A. Sawatzky, Phys. Rev. B **94**, 195127 (2016).

[17] B. Lau and A. J. Millis, Phys. Rev. Lett. **110**, 126404 (2013).

[18] H. Park, A. J. Millis, and C. A. Marianetti, Phys. Rev. Lett. **109**, 156402 (2012).

[19] H. Park, A. J. Millis, and C. A. Marianetti, Phys. Rev. B **89**, 245133 (2014).

[20] A. Subedi, O. E. Peil, and A. Georges, Phys. Rev. B **91**, 075128 (2015).

[21] T. Takimoto, T. Hotta, and K. Ueda, Phys. Rev. B **69**, 104504 (2004).

[22] S. Graser, T. A. Maier, P. J. Hirschfeld, and D. J. Scalapino, New J. Phys. **11**, 025016 (2009).

[23] M. Medarde, P. Lacorre, K. Conder, F. Fauth, and A. Furrer, Phys. Rev. Lett. **80**, 2397 (1998).

[24] S. B. Lee, R. Chen, and L. Balents, Phys. Rev. Lett. **106**, 016405 (2011).

[25] S. B. Lee, R. Chen, and L. Balents, Phys. Rev. B **84**, 165119 (2011).

[26] K. Kubo, Phys. Rev. B **75**, 224509 (2007).

[27] F. Aryasetiawan, K. Karlsson, O. Jepsen, and U. Schönberger, Phys. Rev. B **74**, 125106 (2006).

[28] P. Seth, O. E. Peil, L. Pourovskii, M. Betzinger, C. Friedrich, O. Parcollet, S. Biermann, F. Aryasetiawan, and A. Georges (private communication).

[29] See Supplemental Material at http://link.aps.org/supplemental/10.1103/PhysRevB.95.195117 for further details concerning the disentanglement of orbital and bandwidth effects on the response functions, a comprehensive set of plots for the bulk materials band structures, effects of doping and modified crystal field potentials, and the calculations of response functions in effectively lower dimensional heterostructures. Details on DFT+U calculations for the tendencies of antiferromagnetic ordering inside the monoclinic phase are also reported here.

[30] L. Chen, C. Bourbonnais, T. Li, and A.-M. S. Tremblay, Phys. Rev. Lett. **66**, 369 (1991).

[31] N. Bulut, D. J. Scalapino, and S. R. White, Phys. Rev. B **47**, 2742 (1993).

[32] J. A. Alonso, M. J. Martínez-Lope, M. T. Casais, J. L. García-Muñoz, M. T. Fernández-Díaz, and M. A. G. Aranda, Phys. Rev. B **64**, 094102 (2001).

[33] A. A. Mostofi, J. R. Yates, G. Pizzi, Y.-S. Lee, I. Souza, D. Vanderbilt, and N. Marzari, Comput. Phys. Comm. **185**, 2309 (2014).

[34] P. Blaha, K. Schwarz, G. K. H. Madsen, D. Kvasnicka, and J. Luitz, WIEN2K, *An Augmented Plane Wave + Local Orbitals Program for Calculating Crystal Properties* (Technische Universität Wien, Austria, 2001).

[35] W. Ku, T. Berlijn, and C.-C. Lee, Phys. Rev. Lett. **104**, 216401 (2010).

[36] M. Medarde, C. Dallera, M. Grioni, B. Delley, F. Vernay, J. Mesot, M. Sikora, J. A. Alonso, and M. J. Martínez-Lope, Phys. Rev. B **80**, 245105 (2009).

[37] H. K. Yoo, S. I. Hyun, L. Moreschini, H.-D. Kim, Y. J. Chang, C. H. Sohn, D. W. Jeong, S. Sinn, Y. S. Kim, A. Bostwick, E. Rotenberg, J. H. Shim, and T. W. Noh, Sci. Rep. **5**, 8746 (2015).

[38] D. I. Khomskii, *Basic Aspects of the Quantum Theory of Solids: Order and Elementary Excitations* (Cambridge University Press, Cambridge, 2010).